Available online at www.sciencedirect.com
ScienceDirect
Polar Science 4 (2011) 558–573
NiPR National Institute of Polar Research
http://ees.elsevier.com/polar/

Petrology and mineralogy of the shock-melted H chondrites Yamato–791088 and LaPaz Ice Field 02240

Takafumi Niihara [a,*], Naoya Imae [a,b], Keiji Misawa [a,b], Hideyasu Kojima [a,b]

[a] *Department of Polar Science, The Graduate University for Advanced Studies, 10–3, Midori-cho, Tachikawa-shi, Tokyo 190–8518, Japan*
[b] *Antarctic Meteorite Research Center, National Institute of Polar Research, 10–3, Midori-cho, Tachikawa-shi, Tokyo 190–8518, Japan*

Received 19 February 2010; revised 1 July 2010; accepted 31 August 2010
Available online 22 September 2010

Abstract

We studied the petrology and mineralogy of two types of shock-melted H chondrites: Yamato (Y)–791088 and LaPaz Ice Field (LAP) 02240. Y–791088, which consists of numerous coarse-grained relict phases (40%) and euhedral fine-grained minerals solidified from the shock melt (60%), experienced incomplete melting; a quiescent melt is indicated by the existence of abundant relict phases, pseudomorphed chondrules, and two types of glass. LAP 02240, which consists of small amounts of coarse-grained relict phases (~10%) and fine-grained minerals (~90%), experienced near-complete melting; a rapidly cooled mobilized melt is indicated by the homogeneous compositions of glass and opaque veins.

The homogeneous compositions of relict olivines indicate that the precursors of both chondrites were equilibrated H chondrites. The melting features of Y–791088 and LAP 02240 are very similar to those of Y–790964 (LL) and the fine-grained lithology of Y–790519 (LL), respectively. These two types of shock-melted ordinary chondrites possibly formed *in situ* during dike formation. The quiescent melt is thought to have originated from the injection of shock-heated chondrite blocks into mobilized melt. These two types of melting could have occurred during dike formation on the H chondrite parent body. The textures of the two types of shock melts were not simply affected by the degree of shock melting: they were also controlled by the degree of shear stress.
© 2010 Elsevier B.V. and NIPR. All rights reserved.

Keywords: Y–791088; LAP 02240; Ordinary chondrite; Shock melt; Petrogenesis

1. Introduction

Shock-melted chondrites produced by extensive melting on their parent bodies provide important clues regarding the nature of dynamic shock events such as crater formation on the surface of the parent body and catastrophic disruption of the parent body. Ordinary chondrites may have experienced shock events on their parent bodies, thereby recording shock features such as fracturing, brecciation, degassing, melting, and loss of volatile elements. Based on the mineralogy and petrology of ordinary chondrites, Stöffler et al. (1991) classified the shock stages of such rocks into stages S1–S6, plus the shock-melted stage. Some shock-melted ordinary chondrites experienced near-complete melting that overprinted the original chondritic textures (Y–790519 (LL): Okano et al., 1990; Patuxent Range 91501 (L): Mittlefehldt and Lindstrom, 2001).

* Corresponding author. Tel.: +81 42 512 0709; fax: +81 42 512 3179.
E-mail address: niihara@nipr.ac.jp (T. Niihara).

1873-9652/$ - see front matter © 2010 Elsevier B.V. and NIPR. All rights reserved.
doi:10.1016/j.polar.2010.08.003

Most shock-melted ordinary chondrites contain large amounts of relict minerals and retain chondritic textures; e.g., the H chondrites Y−791088 (Fujimaki et al., 1993), Rose City (Rubin, 1995; Yolcubal and Sack, 1997), Dar al Gani 896 (Folco et al., 2004), and Portales Valley (Kring et al., 1999; Rubin et al., 2001; Ruzicka et al., 2005); the L chondrites Cat Mountain (Kring et al., 1996), Chico (Norman and Mittlefehldt, 2002; Yolcubal and Sack, 1997), and Ramsdorf (Yamaguchi et al., 1999); and the LL chondrite Y−790964 (Okano et al., 1984, 1990; Yamaguchi et al., 1998).

Yamaguchi et al. (1998, 1999) conducted a petrological study of the chondritic regions in Y−790964 (LL) and Ramsdorf (L), and observed abundant "chondrule ghosts" that appear to resemble common objects such as chondrules containing olivine and pyroxene that were crystallized from the shock melt. Fujimaki et al. (1993) reported the presence of pseudomorphed chondrules, similar in texture to "chondrule ghosts", in Y−791088; however, the authors did not describe the detailed textures of the shock melt.

Previous studies have examined the petrology of Y−790964 and paired shock-melted LL chondrites (e.g. Okano et al., 1990; Yamaguchi et al., 1998). Y−790964 comprises coarse-grained (several tens to hundreds of microns in size) relict olivines and chondrule fragments, euhedral pyroxenes, two types of glassy materials, and irregular vesicles in a glassy matrix (Okano et al., 1990; Sato et al., 1982). Y−790519 (LL), which is possibly paired with Y−790964, comprises two different unbrecciated lithologies: a fine-grained (FG) lithology that experienced near-complete melting, and a coarse-grained (CG) lithology comprising relict olivines (several tens to hundreds of microns in size), euhedral pyroxenes, and irregular vesicles in a glassy matrix similar to that in Y−790964 (Okano et al., 1990; Sato et al., 1982). The fayalite (Fa) contents of olivine in the FG lithology do not overlap with the range of Fa values obtained for equilibrated LL chondrites, but are within the range of Fa values obtained for L chondrites (Sato et al., 1982). This FG lithology contains olivine fragments that are several tens of microns in size. The FG and CG lithologies coexist in Y−790519, suggesting that they formed via a single impact event. Sato et al. (1982) and Okano et al. (1990) conducted petrological studies of Y−790519; however, they did not focus on the relationships among different types of shock-melted lithologies.

To clarify the formation conditions of shock-melted chondrites, especially those of H chondrites, we examined the mineralogy and petrology of the shock-melted H chondrites Y−791088 and LAP 02240.

2. Analytical methods

We examined polished thin sections (PTSs) of Y−791088 (91−1; surface area of 78 mm^2) and LAP 02240 (7; surface area of 104 mm^2) together with two shock-melted LL chondrites as reference samples: Y−790964 (81−1) and Y−790519 (73−3). All PTSs were observed using an optical microscope with polarized light for transparent phases and reflected light for opaque phases. The microtextures of all samples were observed using a scanning electron microscope (JEOL JSM−5900 LV) operated at an accelerating voltage of 15 kV. Constituent phases were analyzed using an electron probe microanalyzer (JEOL JXA−8200) operated at an accelerating voltage of 15 kV and electron beam current of 9 nA with a focused beam for minerals, and a current of 3 nA with a defocused beam (10 μm) for glassy phases, to avoid the loss of alkaline elements during analysis. Bence and Albee's correction method (Bence and Albee, 1968) was used for silicates, glasses, and oxides, and the ZAF correction method was used for metals and sulfides. We obtained Raman spectra for glassy phases using a JASCO NRS−1000 Raman microspectrometer operated with a focused laser-beam with a wavelength of 531.91 nm and intensity of 11 mW.

3. Results

3.1. Petrography of Y−791088

The bulk chemical composition of the Y−791088 H chondrite (original mass: 2.1 kg) is in the range of that of H chondrites (Dodd, 1981; Yanai and Kojima, 1995). The interior of Y−791088 is apparently homogeneous, as judged from its monotonous external features. The major constituent phases of Y−791088 and their modal abundances are olivine (39%), pyroxene (28%), opaque minerals of Fe−Ni metals and troilite (23%), glassy phases (8%), and vugs (2%) (Figs. 1a–c, 2–4). The minor minerals are chromites and merrillites. Y−791088 contains coarse-grained lithic fragments (∼40%) in a fine-grained matrix (∼60%). The fragments have irregular shapes and consist of olivine, pyroxene, and Fe−Ni metals rimmed by troilite. The matrix minerals in Y−791088 are the same as those in the lithic fragments. Representative analyses of the constituent phases are listed in Tables 1–5.

3.1.1. Olivine

Olivines in coarse-grained lithic fragments are irregular in shape and are up to ∼1 mm in size (Fig. 2a).

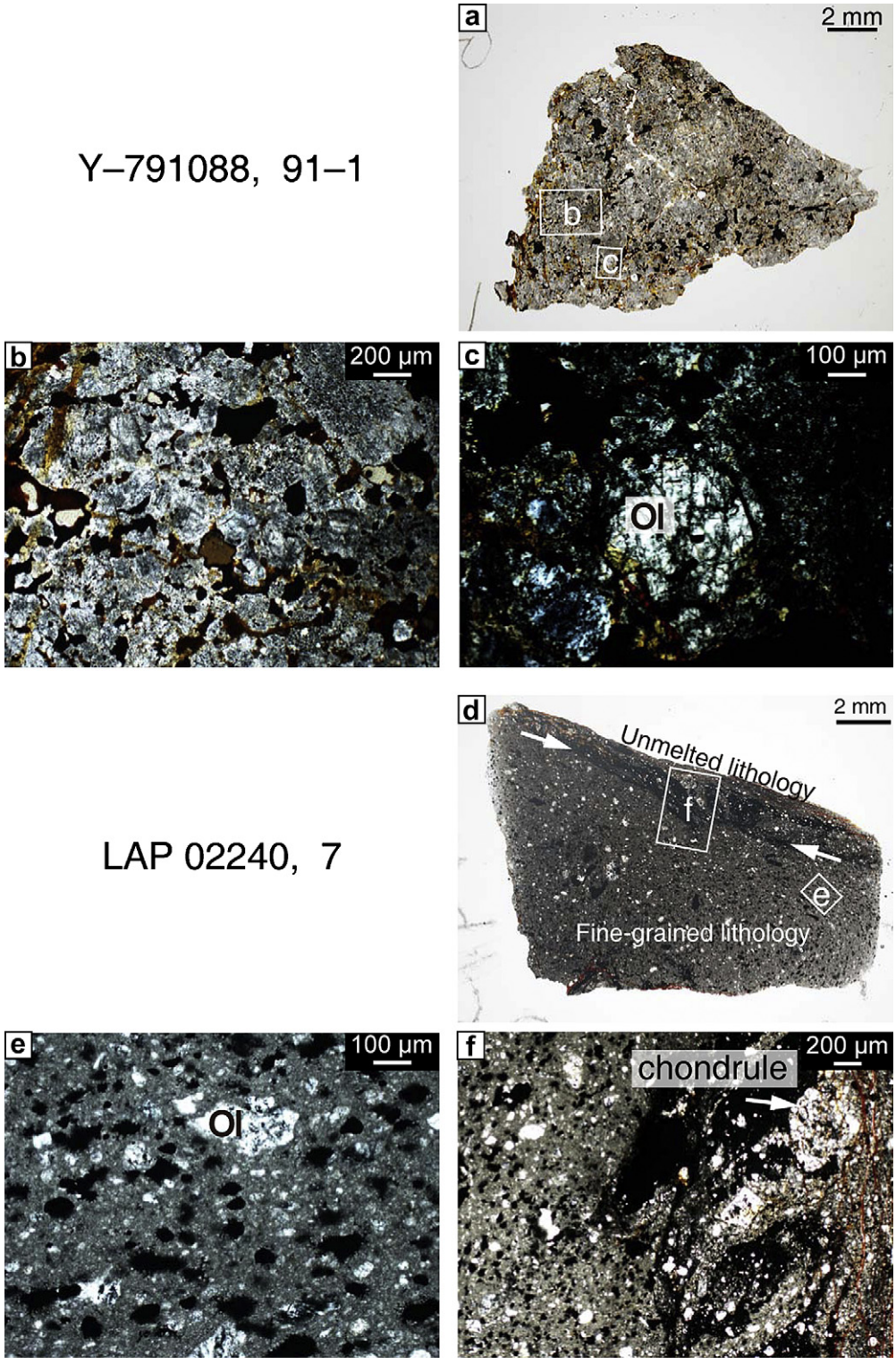

Fig. 1. Photomicrographs of polished thin sections of Y−791088 and LAP 02240 viewed under an optical microscope (transmitted light). (a) Low-magnification image of Y−791088, 91−1. The rectangles indicate the areas shown in (b) and (c). (b) Close-up image of Y−791088. Silicate minerals in Y−791088 show shock darkening caused by numerous fine-grained Fe−Ni metal grains. (c) Transparent region of coarse-grained relict olivine in Y−791088. Transparent olivines are rarely observed and show no shock darkening. (d) LAP 02240, 7. Opaque Fe−Ni−FeS veins

They contain irregular fractures filled with glass and fine-grained Fe–Ni metals (Fig. 2b), and exhibit shock darkening and undulatory extinction under an optical microscope (Fig. 1a–c). The fracture densities of coarse-grained olivines are higher than those of coarse-grained pyroxenes. The chemical compositions of olivines in coarse-grained fragments vary from Fa_{16} to Fa_{21}, with a coefficient of variation (CV) of 3.7% (CaO = ~0.35 wt.%; Cr_2O_3 = 0.1–1.0 wt.%); (Fig. 5a, b). Rare transparent olivine fragments (Fig. 1c) have lower CaO contents (≤0.05 wt.%).

Olivines in the fine-grained matrix are euhedral and ≤20 μm in size (Fig. 2c), and are more heterogeneous in composition (Fa_{17-23}, CV = 5.2%) than coarse-grained olivines, and are slightly more Fe-rich (Fig. 5a, b). Fine-grained olivines contain 0.10–0.35 wt.% CaO.

3.1.2. Pyroxene

Calcium-poor pyroxenes in coarse-grained lithic fragments are irregular in shape and ≤500 μm in size (Fig. 2e). They contain oriented planar fractures filled with glass and fine-grained Fe–Ni metals (Fig. 2f), and show undulatory extinction under an optical microscope. The composition of Ca-poor pyroxenes is $Fs_{11-17}Wo_{1-5}$ (Cr_2O_3 = ~1.4 wt.%) (Fig. 6a).

Pyroxenes in the fine-grained matrix are euhedral and ~30 μm in size (Fig. 2g), showing pronounced zoning in Ca, with higher Ca content in the rim ($Fs_{12-20}Wo_{0.1-31}$; Fig. 2g, Fig. 6b). Compared with coarse-grained pyroxene, the compositional variation in Fe–Mg contents in fine-grained pyroxene shows a wider range and is more ferroan (Fig. 6a, b), with a higher Cr_2O_3 content.

3.1.3. Fe–Ni metals

Fe–Ni metals in coarse-grained lithic fragments, consisting of kamacites and taenites, are irregular in shape and 200–500 μm in size (Fig. 3a). The Ni content of kamacites and taenites is 5–7 and 29–31 wt.%, respectively (Fig. 7a). A coarse-grained plessite (Fig. 3b) has an intermediate composition between kamacite and taenite (Fig. 7a). Coarse-grained Fe–Ni metals are commonly rimmed with troilite.

Fe–Ni metals in the fine-grained matrix are rounded in shape, ~30 μm in size, and rimmed by troilite (Fig. 3c). The Ni content of fine-grained Fe–Ni metals is 7–30 wt.% (Fig. 7b).

3.1.4. Troilite

Troilites in coarse-grained fragments are irregular or rectangular in shape and up to ~600 μm in size, although we identified only two grains (Fig. 3d). Fine-grained, rounded Fe–Ni metals in the matrix are rimmed by troilite grains of ~5 μm in size (Fig. 3c).

3.1.5. Glassy phases

Glassy phases occur in the interstices of minerals and comprise clear and dusty portions when viewed under an optical microscope (Fig. 4). Clear glasses coexist with minor amounts of chromite and merrillite, and they exist in the interstices of fine-grained olivines (Fig. 4a). Dusty glasses are brown in color and occur near euhedral and rectangular pyroxenes (Fig. 4b). The two types of glass are albitic in composition (Fig. 8; Table 4) and generally do not coexist. The potassium content of clear glass is higher (K_2O = ~2 wt.%) than that of dusty glass (K_2O = ~0.1 wt.%) (Fig. 8). Raman spectra indicate that the dusty glass contains fine-grained plagioclase (Fig. 9).

3.1.6. Chromite and merrillite

Chromites (up to 2 μm in size) and merrillites (up to ~40 μm in size), both of which are minor minerals, are embedded in clear glass (Fig. 3e, f). Chromites are brown in color and usually tetrahedral in shape; others are anhedral. The compositions of chromites are similar to those of chromites in other H chondrites (Table 5; Krot et al., 1993). Merrillites coexist with Fe–Ni metals (Fig. 3f).

3.1.7. Chondrules and pseudomorphed chondrules

Two barred-olivine (BO) chondrules are identified in the PTS of Y–791088 (Fig. 2d). The compositions of olivines in BO chondrules are similar to those of coarse-grained olivines (Fa_{16-20}, CaO = 0.15–0.28 wt.%; Cr_2O_3 = 0.1–0.6 wt.%; Fig. 5c, d).

Rounded objects, consisting of euhedral olivine and pyroxene with interstitial glass, appear to resemble chondrules (Fig. 2h). We refer to these objects as "pseudomorphed chondrules" (Fujimaki et al., 1993). We observed seven porphyritic olivine (PO) chondrules and

are indicated by arrows. Opaque veins mark the boundary between unmelted and melted lithologies. The rectangles indicate the areas shown in (e) and (f). (e) Close-up image of LAP 02240. Relict olivines are embedded in a fine-grained matrix that consists of euhedral or dendritic olivines and pyroxenes, and Fe–Ni droplets. (f) Boundary region between shock-melted and unmelted areas in LAP 02240. Note the elongated chondrule. Ol: Olivine.

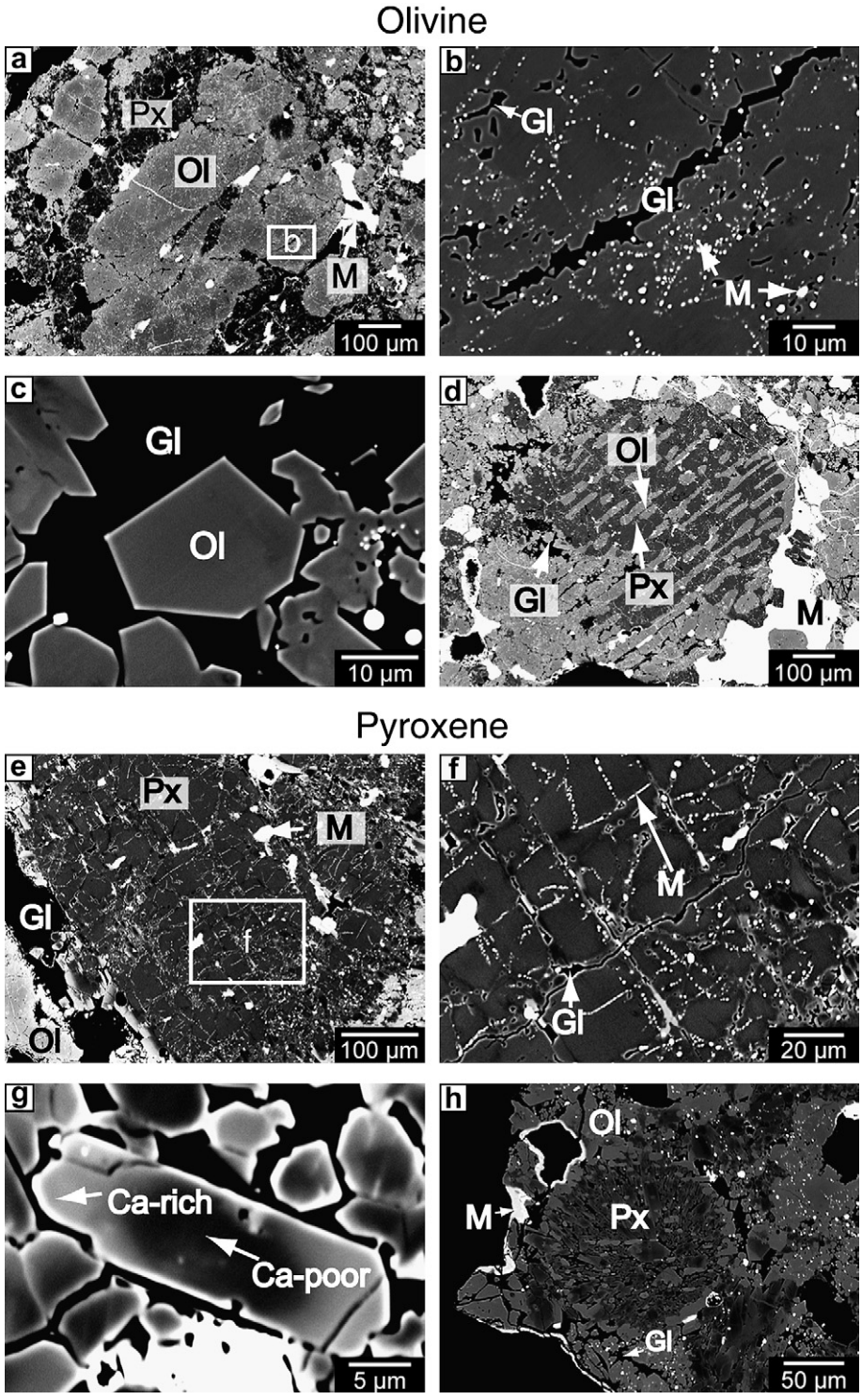

Fig. 2. Back-scattered electron images of olivine and pyroxene in Y−791088. (a) Low-magnification image of relict olivine; such grains are irregular in shape. (b) High-magnification image of the area outlined by the white rectangle in (a), showing overgrowths of olivine and the occurrence of numerous fine-grained metal droplets along fractures. (c) Close-up image of olivine in the shock-melted region. Olivine grains that crystallized from shock melt are euhedral and embedded in glass. (d) Relict barred-olivine chondrule that retains its original rounded shape and texture. (e) Low-magnification image of relict pyroxene; such grains are irregular in shape. (f) High-magnification image of the area outlined by

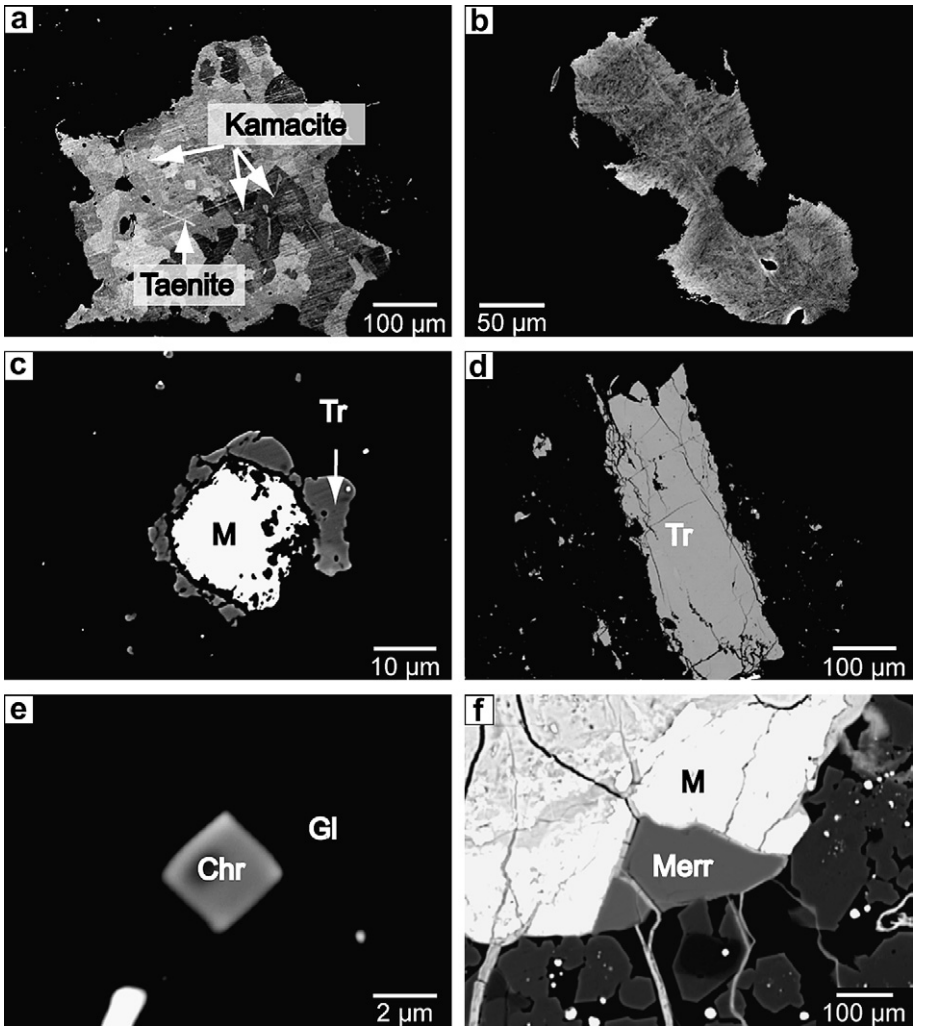

Fig. 3. Back-scattered electron images of Fe–Ni metal, troilite, chromite, and merrillite in Y–791088. (a) Coarse-grained relict Fe–Ni metal. The interior is irregular in shape, mostly consisting of kamacite, with rare taenite needles. (b) Coarse-grained plessite showing a very fine-grained internal texture. (c) Fine-grained Fe–Ni metal droplet surrounded by troilite, which is embedded in glass and caused shock darkening of relict olivine and pyroxene. The metal droplets solidified from the shock melt. (d) Coarse-grained relict troilite. (e) Fine-grained euhedral chromite embedded in glass. (f) Merrillites occur near Fe–Ni metals and are embedded in glass. M: Fe–Ni metal. Tr: Troilite. Chr: Chromite. Merr: Merrillite. Gl: Glass.

seven fine-grained pyroxene pseudomorphed chondrules. The olivines in PO pseudomorphed chondrules (Fa_{15-22}, CaO = 0.1–0.3 wt.%; Cr_2O_3 = 0.2–0.8 wt.%; Fig. 5c, d) have compositions similar to those of fine-grained olivines. The pyroxenes in BO chondrules ($Fs_{15-17}Wo_{1-2}$) are more homogeneous in composition than pyroxenes in fine-grained pyroxene pseudomorphed chondrules (Fig. 6c, d). The Ca content of pyroxenes in fine-grained pseudomorphed chondrules increases from core to rim ($Fs_{11-20}Wo_{0-30}$; Fig. 6d). The Cr content of pyroxenes in BO chondrules (Cr_2O_3 = ~0.4 wt.%) is lower than that of fine-grained pyroxene pseudomorphed chondrules (Cr_2O_3 = ~1.8 wt.%; Table 2).

3.2. Petrography of LAP 02240

The paired shock-melted H chondrites LAP 02240 (original mass: 28 g), LAP 04614, and LAP 04745

the white rectangle in (e). Relict pyroxenes contain planar fractures. Numerous fine-grained Fe–Ni metal droplets occur along fractures. (g) Close-up image of euhedral pyroxene in the shock-melt region, showing normal Ca-zoning. (h) Fine-grained pseudomorphed chondrule with a rounded shape. Pyroxenes are euhedral, as in the shock-melt region. Ol: Olivine. Px: Pyroxene. M: Fe–Ni metals. Gl: Glass.

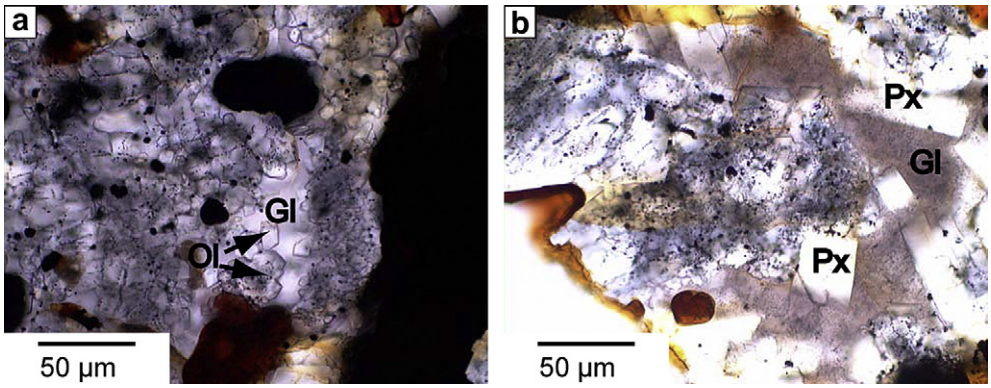

Fig. 4. Transmitted light photographs of glassy phases. (a) Clear portion in Y–791088. Euhedral olivines occur interstitially. (b) Dusty portion in Y–791088. Euhedral pyroxene is embedded in dusty glass. Gl: Glass. Ol: Olivine. Px: Pyroxene.

were recovered from Antarctica (Satterwhite and Righter, 2004). LAP 02240 consists of melted and unmelted lithologies divided by opaque veins of Fe–Ni metals and troilite. These veins are ~1 mm thick and cut across the PTS of LAP 02240 (Fig. 1d). The major constituent phases in the LAP 02240 shock-melted lithology and their modal abundances are olivine (35%), pyroxene (25%), opaque minerals of Fe–Ni metals and troilite (22%), glass (14%), and cavities (4%). The minor minerals are chromite and merrillite. The melted lithology is uniformly dark in color (Fig. 1d, e). Two elongate PO chondrules are identified in the unmelted lithology, adjacent to the vein (Fig. 1f). The melted lithology consists mainly of fine-grained matrix (~90%) and coarse-grained olivines with irregularly shaped Fe–Ni metals (~10%) (Fig. 1e). Silicates in the fine-grained matrix consist of olivine and pyroxene that coexist with glass.

3.2.1. Olivine

Olivines in coarse-grained lithic fragments are irregular or rounded in shape, up to 400 μm in size, and commonly accompany fractures (Fig. 10a) filled with glass and fine-grained Fe–Ni metals. Coarse-grained olivines are transparent in their interior and show undulatory extinction under an optical microscope. The coarse-grained olivines show a limited range of compositions: $Fa_{18–20}$ with CV = 2.2% (CaO = ~0.15 wt.%; Cr_2O_3 = ~0.2 wt.%; Fig. 5e, f; Table 1). Olivines in the

Table 1
Representative analyses of olivines (wt.%).

	Y–791088				LAP 02240			
	Relicts	Melt matrix	Chondrules		Relicts	Melt matrix	Chondrules	
			BO[a]	PO[b]			BO[a]	PO[c]
SiO_2	39.0 (0.2)	37.7 (0.2)	39.0 (0.2)	38.7 (0.2)	39.3 (0.2)	39.3 (0.2)	39.2 (0.2)	39.5 (0.2)
TiO_2	0.01 (0.01)	0.03 (0.03)	0.03 (0.03)	0.02 (0.02)	0.09 (0.04)	0.05 (0.03)	0.00	0.06 (0.03)
Al_2O_3	0.00	0.00	0.01 (0.01)	0.01 (0.01)	0.00	0.01 (0.01)	0.00	0.01 (0.01)
Cr_2O_3	0.17 (0.04)	0.37 (0.05)	0.31 (0.04)	0.74 (0.05)	0.00	0.06 (0.04)	0.08 (0.04)	0.02 (0.02)
FeO	16.8 (0.4)	19.3 (0.4)	16.7 (0.4)	18.9 (0.4)	17.5 (0.4)	17.0 (0.4)	17.0 (0.4)	17.3 (0.4)
MnO	0.45 (0.01)	0.38 (0.08)	0.43 (0.09)	0.50 (0.08)	0.60 (0.09)	0.46 (0.08)	0.37 (0.08)	0.56 (0.08)
MgO	43.5 (0.2)	41.1 (0.2)	43.3 (0.3)	40.9 (0.3)	42.8 (0.2)	42.8 (0.2)	43.3 (0.2)	42.5 (0.2)
CaO	0.05 (0.05)	0.20 (0.01)	0.22 (0.01)	0.25 (0.02)	0.04 (0.01)	0.10 (0.02)	0.04 (0.01)	0.03 (0.01)
Na_2O	0.00	0.01 (0.01)	0.02 (0.02)	0.00	0.00	0.00	0.00	0.03 (0.03)
K_2O	0.00	0.00	0.00	0.00	0.00	0.00	0.00	0.01 (0.01)
P_2O_5	0.02 (0.02)	0.95 (0.08)	0.00	0.03 (0.03)	0.02 (0.02)	0.00	0.00	0.00
Total	100.0	100.0	100.0	100.1	100.4	99.8	100.0	100.0
Fa	17.8	20.9	17.8	20.6	18.6	18.2	18.0	18.6

Figures in parentheses are the 1σ values calculated for the analyses.
[a] Barred olivine chondrule (relict).
[b] Porphyritic olivine chondrule (shock-melted).
[c] Porphyritic olivine chondrule (outside of shock-melt).

Table 2
Representative analyses of pyroxenes (wt.%).

	Y–791088						LAP 02240		
	Relicts	Melt matrix		Chondrules			Melt matrix		Chondrule
		Rim	Core	BO[a]	Fine-grained		Rim	Core	BO[a]
					Rim	Core			
SiO_2	56.0 (0.2)	52.6 (0.2)	56.3 (0.2)	55.7 (0.2)	52.4 (0.2)	55.8 (0.2)	55.4 (0.2)	56.7 (0.3)	55.0 (0.3)
TiO_2	0.14 (0.04)	0.41 (0.05)	0.04 (0.04)	0.27 (0.04)	0.42 (0.05)	0.19 (0.04)	0.10 (0.04)	0.20 (0.03)	0.28 (0.04)
Al_2O_3	0.34 (0.03)	1.64 (0.06)	0.17 (0.03)	0.41 (0.03)	2.37 (0.06)	0.29 (0.03)	0.40 (0.03)	0.12 (0.03)	1.17 (0.05)
Cr_2O_3	0.36 (0.04)	1.45 (0.06)	0.36 (0.04)	0.38 (0.04)	1.77 (0.06)	0.30 (0.04)	1.51 (0.07)	0.14 (0.04)	1.04 (0.06)
FeO	10.9 (0.3)	7.5 (0.3)	10.3 (0.3)	10.9 (0.3)	7.2 (0.3)	10.5 (0.3)	10.8 (0.3)	10.6 (0.3)	11.0 (0.3)
MnO	0.27 (0.08)	0.45 (0.08)	0.46 (0.09)	0.47 (0.08)	0.48 (0.08)	0.55 (0.08)	0.40 (0.09)	0.43 (0.08)	0.33 (0.08)
MgO	31.1 (0.2)	19.9 (0.2)	31.6 (0.2)	31.2 (0.2)	19.4 (0.2)	31.7 (0.2)	29.2 (0.2)	30.9 (0.2)	29.9 (0.2)
CaO	0.86 (0.03)	14.9 (0.1)	0.80 (0.02)	0.73 (0.02)	14.11 (0.09)	0.71 (0.02)	2.66 (0.04)	0.64 (0.02)	1.32 (0.03)
Na_2O	0.03 (0.02)	0.40 (0.03)	0.04 (0.02)	0.02 (0.02)	0.49 (0.03)	0.04 (0.02)	0.22 (0.03)	0.04 (0.02)	0.03 (0.03)
K_2O	0.01 (0.01)	0.00	0.00	0.02 (0.01)	0.03 (0.01)	0.00	0.02 (0.01)	0.00	0.00
P_2O_5	0.03 (0.03)	0.00	0.04 (0.03)	0.00	0.05 (0.04)	0.02 (0.02)	0.00	0.00	0.04 (0.04)
Total	100.0	99.3	100.1	100.1	98.7	100.1	100.7	99.8	100.1
Fs	16.1	12.0	15.2	16.1	12.0	15.4	16.3	15.9	16.7
Wo	1.6	30.7	1.5	1.4	30.2	1.3	5.2	1.2	2.6

Figures in parentheses are the 1σ values calculated for the analyses.
[a] In barred-olivine chondrule.

fine-grained matrix are euhedral, subhedral, or dendritic in shape and up to ~5 μm in size (Fig. 10b). Their composition is $Fa_{14–20}$ (CV = 9.2%), being more heterogeneous in composition than the coarse-grained olivines (Table 1). The Fa content of fine-grained olivines is slightly more magnesian than that of coarse-grained olivines (Fig. 5e, f). The contents of the minor elements Ca and Cr in fine-grained olivines (CaO = ~0.3 wt.%; Cr_2O_3 = ~0.9 wt.%) are higher than those in coarse-grained olivines (Fig. 5e, f).

3.2.2. Pyroxene

Pyroxenes in the fine-grained matrix are euhedral and ~30 μm in size (Fig. 10b). The CaO content of pyroxenes increases from core to rim ($Fs_{11–17}Wo_{1–7}$; Fig. 6e). We observed no high-Ca pyroxene or coarse-grained low-Ca pyroxene.

3.2.3. Fe–Ni metals

Small numbers of coarse-grained, irregularly shaped Fe–Ni metals (400–600 μm in size) occur in the matrix, rimmed in part with troilite (Fig. 10c). Most of these grains are martensite, with minor plessite. The Ni content of martensite is 6–10 wt.% (Fig. 7c). Iron-Ni metals in the fine-grained matrix are rounded in shape and ~50 μm in size; they are commonly rimmed by troilite (Fig. 10d). The range of Ni content (5–10 wt.%; Fig. 7d) in Fe–Ni metals is smaller than that in Y–791088 (5–30 wt.%; Fig. 7b).

Table 3
Representative analyses of Fe–Ni metals and troilites (wt.%).

	Fe–Ni metal							Troilite	
	Y–791088					LAP 02240		Y–791088	LAP 02240
	Coarse-grained			Fine-grained		Coarse-grained	Fine-grained		
	Ni-rich[a]	Plessite	Ni-poor	Ni-rich	Ni-poor				
Si	0.01 (0.01)	0.02 (0.01)	0.00	0.00	0.00	0.01 (0.01)	0.00	0.03 (0.01)	0.01 (0.01)
Cr	0.06 (0.03)	0.05 (0.03)	0.00	0.08 (0.03)	0.01 (0.01)	0.07 (0.03)	0.04 (0.03)	0.26 (0.03)	0.21 (0.03)
S	0.03 (0.01)	0.01 (0.01)	0.00	0.04 (0.01)	0.00	0.02 (0.01)	0.01 (0.01)	36.07 (0.11)	36.03 (0.11)
Co	0.13 (0.02)	0.29 (0.03)	0.48 (0.04)	0.35 (0.03)	0.47 (0.04)	0.44 (0.04)	0.49 (0.04)	0.00	0.00
Fe	52.5 (0.3)	84.0 (0.4)	93.2 (0.4)	73.6 (0.4)	91.9 (0.4)	92.8 (0.4)	91.1 (0.4)	62.8 (0.4)	62.8 (0.4)
Cu	0.09 (0.04)	0.08 (0.05)	0.00	0.09 (0.05)	0.05 (0.05)	0.06 (0.05)	0.00	0.11 (0.01)	0.10 (0.05)
Ni	31.4 (0.2)	15.8 (0.2)	6.7 (0.1)	26.1 (0.2)	7.5 (0.1)	7.0 (0.1)	8.4 (0.1)	0.07 (0.04)	0.34 (0.04)
Total	84.2	100.3	100.4	100.3	99.9	100.4	100.0	99.3	99.5

Figures in parentheses are the 1σ values calculated for the analyses.
[a] Thin Ni-rich needle in coarse-grained metal.

Table 4
Representative analyses of glasses (wt.%).

	Y−791088		LAP 02240
	Dusty	Clear	Clear
SiO_2	65.5 (0.5)	67.8 (0.5)	65.2 (0.5)
TiO_2	0.41 (0.08)	0.48 (0.08)	0.02 (0.06)
Al_2O_3	19.7 (0.3)	17.0 (0.3)	21.3 (0.3)
Cr_2O_3	0.00	0.10 (0.07)	0.00
FeO	1.4 (0.2)	1.5 (0.2)	1.5 (0.3)
MnO	0.00	0.00	0.00
MgO	0.36 (0.05)	0.5 (0.05)	0.49 (0.05)
CaO	3.23 (0.08)	1.66 (0.06)	2.92 (0.08)
Na_2O	9.0 (0.3)	7.9 (0.3)	10.4 (0.3)
K_2O	0.07 (0.02)	1.84 (0.06)	0.10 (0.03)
P_2O_5	0.4 (0.2)	1.1 (0.2)	0.2 (0.1)
Total	100.1	99.9	102.1

Figures in parentheses are the 1σ values calculated for the analyses.

3.2.4. Minor phases: troilite, glass, chromite, and merrillite

Troilites ($\sim$10 μm in size) coexist with fine-grained Fe−Ni metals (Fig. 10d). Homogeneous potassium-poor glassy phases occur in mineral interstices ($K_2O = \sim$0.10 wt.%; Fig. 8 and Fig. 10b). Chromites are irregular or tetrahedral in shape, 2 μm in size, and are generally embedded in glass. Aggregates of fine-grained chromite occur in coarse-grained olivine (Fig. 10e). The composition of chromite is similar to that of chromite in H chondrites (Krot et al., 1993; Table 5). Fine-grained merrillites ($\leq$50 μm in size) coexist with Fe−Ni metals embedded in glass (Fig. 10f).

3.2.5. Chondrule

An elongated BO chondrule is observed in the FG lithology (Fig. 10g). The mesostasis of the BO chondrule is replaced by glass with fine-grained olivines (Fa_{17-19}, CaO = $\sim$0.1 wt.%) and pyroxenes (Fig. 5g, h; Table 1).

Table 5
Representative analyses of chromites and merrillites (wt. %).

	Chromite		Merrillite	
	Y−791088	LAP 02240	Y−791088	LAP 02240
SiO_2	0.06 (0.03)	0.00	0.03 (0.03)	0.00
TiO_2	1.68 (0.06)	1.90 (0.08)	0.00	0.06 (0.04)
Al_2O_3	6.3 (0.1)	6.5 (0.1)	0.05 (0.02)	0.01 (0.01)
Cr_2O_3	58.3 (0.3)	56.4 (0.3)	0.02 (0.02)	0.00
FeO	22.7 (0.4)	27.6 (0.5)	1.6 (0.1)	0.7 (0.1)
MnO	0.6 (0.1)	1.0 (0.1)	0.11 (0.06)	0.02 (0.02)
MgO	7.1 (0.1)	3.38 (0.08)	3.67 (0.08)	3.68 (0.08)
CaO	0.01 (0.01)	0.02 (0.01)	47.5 (0.2)	47.2 (0.2)
Na_2O	0.03 (0.03)	0.03 (0.03)	2.6 (0.1)	2.46 (0.09)
K_2O	0.00	0.02 (0.01)	0.02 (0.01)	0.06 (0.01)
P_2O_5	0.03 (0.03)	0.01 (0.01)	44.8 (0.6)	45.7 (0.6)
Total	96.8	96.9	100.4	99.9

Figures in parentheses are the 1σ values calculated for the analyses.

4. Discussion

4.1. Two types of shock-melted H chondrites

4.1.1. Y−791088, incompletely melted H chondrite under quiescent conditions

Coarse-grained lithic fragments in Y−791088 are relict phases characterized by various shock features such as undulatory extinction and disturbed chemical zoning. The Fa contents of relict olivines in Y−791088 are within the range of those in H4−6 chondrites (Fig. 5a,b). The CaO contents of shock-darkened olivines ($\leq$0.35 wt.%) are much higher than those in H4−6 chondrites (<0.05 wt.%), and are similar to those of olivines crystallized from shock melt and olivines in unequilibrated ordinary chondrites (e.g., Kimura et al., 2002; Scott and Taylor, 1983), whereas coarse-grained olivines without shock-darkening (Fig. 1c) contain lower concentrations of CaO (<0.05 wt.%). Yamaguchi et al. (1999) observed a similar chemical trend in relict olivines in the Ramsdorf L chondrite, and suggested that the chemical compositions were affected by impact melting events. The fracture densities in coarse-grained shock-darkened olivines are higher than those in pyroxenes. Overgrown olivines occur along fractures and coexist with glass (Fig. 2b). The enrichment of Ca in coarse-grained shock-darkened olivines may be derived from these overgrowths of olivines (Table 1).

Relict olivine grains are highly fractured compared with relict low-Ca pyroxene grains. The chemical composition of the latter is identical to that of low-Ca pyroxenes in equilibrated H chondrites. Iron-Ni metals in H chondrites generally consist of two distinct phases of kamacite and taenite. Several kamacite phases are recognized in Y−791088 (Fig. 3a). Kamacite grains in coarse-grained Fe−Ni metals (Fig. 3) would have been disturbed by the subsolidus reaction with taenite graines during shock heating.

The FG lithology consists of euhedral olivine, pyroxene, glass, and chromite along with rounded Fe−Ni metals with sulfide rims, and shows igneous textures. Fine-grained minerals and Fe−Ni metal droplets could have rapidly solidified from the shock melt (Fig. 2c, g, and Fig. 3c, e). The Ni contents in fine-grained Fe−Ni metals included in coarse-grained olivines and low-Ca pyroxenes vary from 7 to 30 wt.% (Fig. 7b), indicating that metal grains did not originate from the products of a subsolidus reduction of relict olivine or low-Ca pyroxene; instead, they were solidified from the shock melts. Olivines and low-Ca pyroxenes show shock darkening due to the injection of fine-grained Fe−Ni metal droplets.

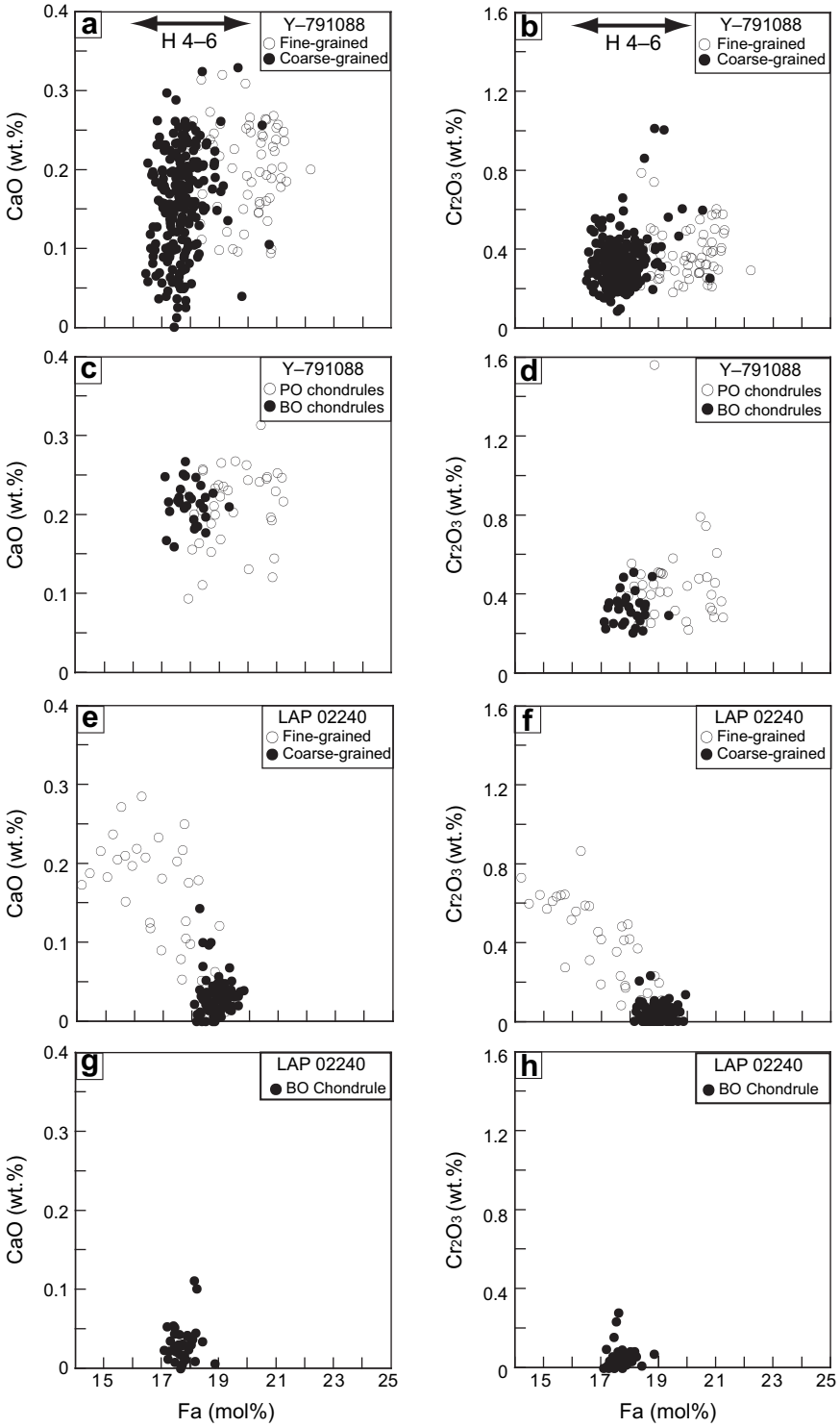

Fig. 5. Plots of Fa (mol%) vs. CaO and Cr_2O_3 (wt.%) in olivine. (a) Fa vs. CaO for a coarse-grained fragment (relict) and fine-grained olivine crystallized from shock melt in Y−791088. Fayalite contents in relict olivines are within the range of those in equilibrated H chondrites. Olivine crystallized from shock melt has a more ferroan composition than do olivine fragments. CaO contents are variable. (b) Fa vs. Cr_2O_3 for relict olivines and olivine crystallized from shock melt in Y−791088. (c) Fa vs. CaO for olivines in BO chondrules and PO pseudomorphed chondrule in Y−791088. The composition of olivine in BO chondrules is similar to that of olivine relicts. The PO pseudomorphed chondrules show a similar trend to that of olivine crystallized from shock melt. (d) Fa vs. Cr_2O_3 for barred-olivine chondrules and PO pseudomorphed chondrules in

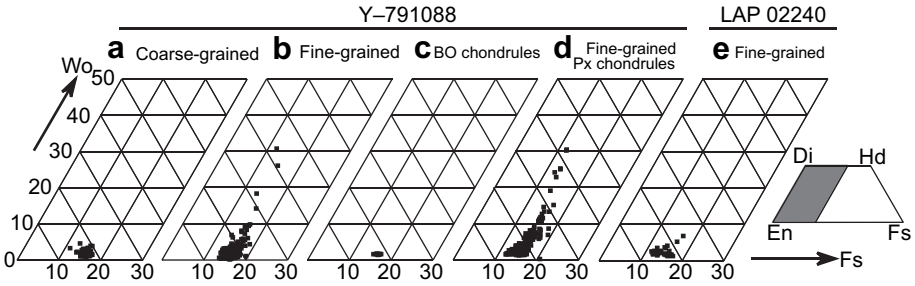

Fig. 6. Pyroxene compositional data (atomic ratio). (a) Relict fragments in Y−791088 have homogeneous compositions. (b) Pyroxene crystallized from shock melt in Y−791088, showing Ca zoning, with increasing Ca content from core to rim. (c) Pyroxenes in BO chondrule mesostasis in Y−791088, showing a homogeneous composition similar to that of relict olivines. (d) Pyroxenes in fine-grained pseudomorphed chondrule in Y−791088, showing chemical zoning similar to that of pyroxene in shock melt. (e) Pyroxenes crystallized from shock melt in LAP 02240, showing weak zoning in Ca. Px: Pyroxene. En: Enstatite. Di: Diopside. Hd: Hedenbergite. Fs: Ferrosilite. Wo: Wollastnite.

Two BO chondrules found in Y−791088 (Fig. 2d) are clearly relict chondrules (not crystallized from shock melt), because their textures are very similar to those of BO chondrules in other ordinary chondrites. In addition, the compositions of olivines in the BO chondrules are indistinguishable from those of coarse-grained relict olivines (Fig. 5c, d). Most other pseudomorphed chondrules comprise fine-grained olivines and low-Ca pyroxenes with glass. The compositional trends of olivines and low-Ca pyroxenes in pseudomorphed chondrules (Fig. 2h) are similar to those in the fine-grained matrix (Figs. 5 and 6), indicating that the former could have crystallized from the shock melt and that their rounded shapes could represent remnants of pre-existing chondrules. The observed textures, homogeneous compositions of olivines and pyroxenes, and presence of relict BO chondrules indicate that the pre-impact material of Y−791088 had been metamorphosed; i.e. an H4 or H5 chondrite.

Y−791088 contains two types of glassy phases: feldspathic glass (K_2O = ∼2 wt.%) and dusty glass containing fine-grained plagioclase (K_2O = ∼0.1 wt.%) (Fig. 8). These two phases may reflect the chemical heterogeneity of precursor materials, suggesting that the shock melt of Y−791088 was not well mixed or homogenized; i.e., it was kept quiescent. This interpretation is supported by the presence in Y−791088 of relict phases and pseudomorphed chondrules with rounded shapes.

Close resemblances are found among the shock-melted Y−790964 (LL) and the CG lithologies of Y−790519 (LL) and Y−791088 (H): they show coarse-grained textures with pseudomorphed chondrules, and contain two types of glassy materials and a lesser amount of Fe−Ni metal droplets solidified from shock melts (Fig. 11). Fine-grained olivines crystallized from the shock melt are more ferroan in composition than are relict coarse-grained olivines (Okano et al., 1990; Sato et al., 1982), suggesting that an analogous process, which formed quiescent melts, occurred in the parent bodies of Y−791088 (H) and Y−790519/Y−790964 (LL).

4.1.2. LAP 02240, completely melted H chondrite under mobilization

Coarse-grained olivines in LAP 02240 are relict, as indicated by their irregular shapes, undulatory extinction, irregular fractures filled with glass and fine-grained Fe−Ni metals, and homogeneous compositions. The relict olivines differ from the coarse-grained olivines in Y−791088 in that they contain fewer Fe−Ni metal droplets and show no evidence of significant shock-darkening (Fig. 1e). These observations suggest that the fracturing of olivines and injection of metals into olivine grains did not occur in LAP 02240. The CaO contents of relict olivines in LAP 02240 are <0.1 wt.% (Fig. 5), which overlaps with the compositional range of equilibrated H chondrites. Fine-grained olivines and low-Ca pyroxenes show euhedral or dendritic textures, suggesting crystallization from shock melt. The fine-grained olivines are more magnesian in composition than are relict olivines (Fig. 5e, f).

A BO chondrule buried in the shock melt (Fig. 10g) is considered a relict, based on its texture and the observation of undulatory extinction. The compositions of chondrule olivines are identical to those of relict olivines

Y−791088. (e) Fa vs. CaO for relict olivines and olivine crystallized from shock melt in LAP 02240. Olivine crystallized from shock melt has a more magnesian composition than does relict olivine. (f) Fa vs. Cr_2O_3 for relict olivines and olivine crystallized from shock melt in LAP 02240. (g) Fa vs. CaO for a relict barred-olivine chondrule in LAP 02240. The composition of olivine in the BO chondrule is similar to that of relict olivines. (h) Fa vs. Cr_2O_3 for a relict barred-olivine chondrule in LAP 02240.

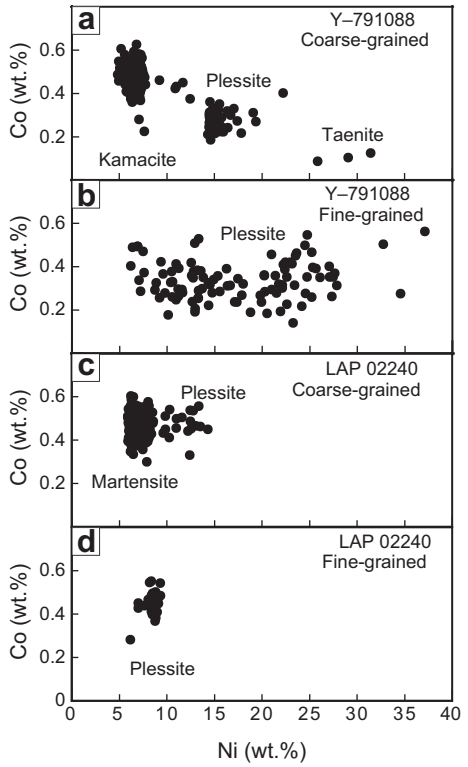

Fig. 7. Compositional variations in Fe–Ni metals. (a) Coarse-grained fragments in Y–791088, which plot in the compositional fields of taenite, plessite, and kamacite. The plessite has intermediate compositions between kamacite and taenite. (b) Fine-grained droplets in Y–791088, showing a wide range of Ni compositions. (c) Coarse-grained fragments in LAP 02240, containing martensite and plessite. (d) Fine-grained droplets in LAP 02240, showing overlapping compositions with coarse-grained Fe–Ni metals in LAP 02240.

(Fig. 5g, h). The high degree of melting meant that the original chondritic textures were not preserved. The presence of a relict fragment of chondrule, as well as relict olivine grains with homogeneous compositions, suggests that thermal metamorphism ceased prior to the shock melting.

The FG lithology of the Y–790519 LL chondrite (Fig. 11) and LAP 02240 show similar petrological and

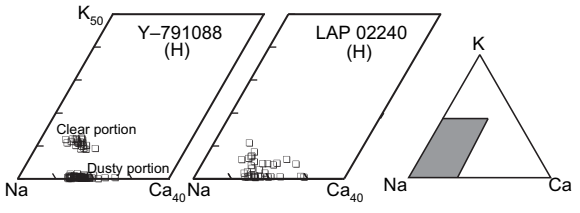

Fig. 8. Chemical compositions of glassy phases (atomic ratio). The dusty portion in Y–791088 is K-poor, and the clear portion is K-rich. Glasses in LAP 02240 are more homogeneous in K components than are those in Y–791088. Na: sodium. K: Potassium. Ca: Calcium.

mineralogical characteristics: the existence of opaque veins of Fe–Ni metals and troilite, abundant Fe–Ni droplets solidified from the shock melt, dominant fine-grained texture, and magnesian compositional trends of fine-grained olivines (Okano et al., 1990; Sato et al., 1982). In LAP 02240, opaque veins that contain an elongated PO chondrule occur at the boundary of the shock melt and the host chondrite. Stöffler et al. (1991) described similar relationships in small dikes and melt veins in shocked chondrites, and suggested, by analogy to terrestrial impact craters, that the opaque veins and silicate melt formed in intrusive dikes affected by a single impact event.

The presence of flow texture and an elongated PO chondrule (Fig. 1d) indicate that the shock melt was mobilized before or during solidification.

4.2. Comparison of Y–791088 and LAP 02240

Olivines ($Fa_{17–23}$) and pyroxenes ($Fs_{12–20}$) in the fine-grained matrix of Y–791088 are more heterogeneous in composition and more ferroan than are coarse-grained relict olivines and pyroxenes (Figs. 5 and 6). Fine-grained olivines that rapidly crystallized from the shock melt of LAP 02240 are more magnesian than are relict olivines. The magnesian trend of fine-grained olivines in LAP 02240 is in contrast to the ferroan trend of fine-grained olivines in Y–791088 (Fig. 5) and in Y–790519 (Sato et al., 1982). The mobilized melt of LAP 02240 may have crystallized under a slightly reducing condition compared with the quiescent melt of Y–791088. The modal abundance of metals in the shock-melt region of Y–791088 (19%) is slightly less than that in LAP 02240 (22%). The relatively magnesian compositions of fine-grained olivines and slightly magnesian low-Ca pyroxenes in LAP 02240 may reflect the higher modal abundance of Fe–Ni metals. Opaque

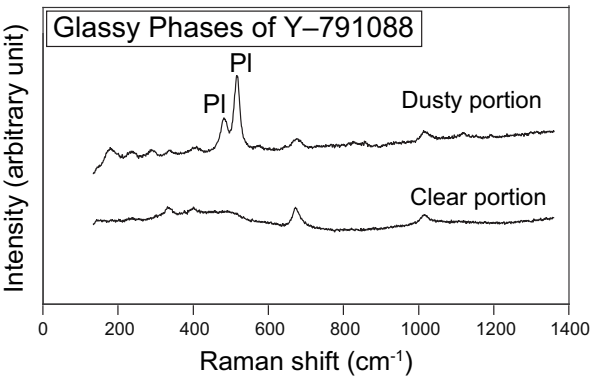

Fig. 9. Raman spectra of glassy phases. Dusty glasses in Y–791088 contain fine-grained plagioclase. Pl: Plagioclase.

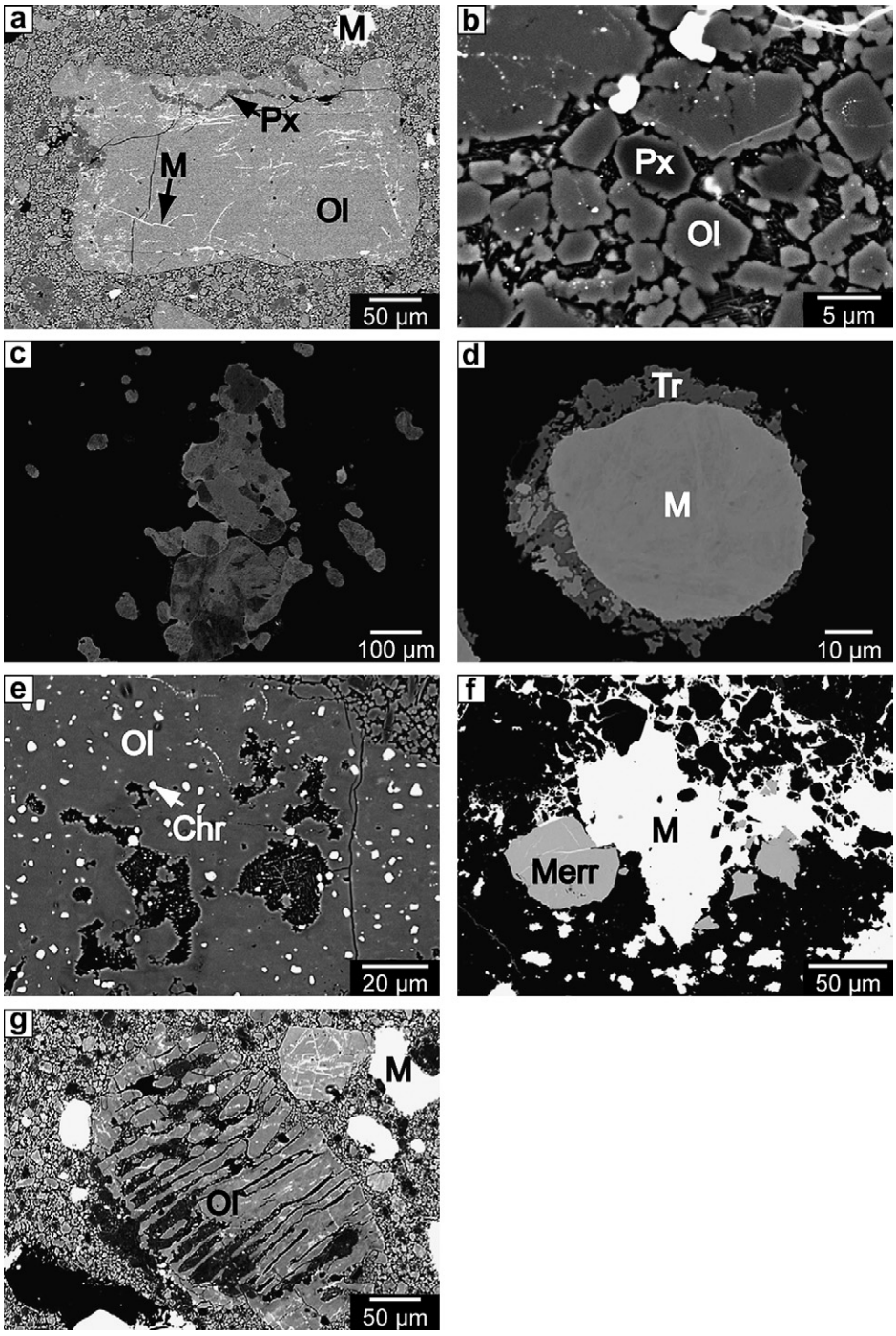

Fig. 10. Back-scattered electron images of LAP 02240. (a) Relict olivine is irregular in shape and contains numerous fine-grained Fe–Ni metal droplets. (b) Melt matrix showing igneous texture. Olivines and pyroxenes are euhedral or dendritic in shape. (c) Coarse-grained Fe–Ni metal fragment. The grain boundary is unclear. (d) Fine-grained Fe–Ni metal droplet surrounded by a troilite rim. The mean grain size of the metal droplets is larger than that in Y–791088. (e) Euhedral chromite coexisting with a relict olivine grain. (f) Merrillite occurring near Fe–Ni metals and embedded in glass. (g) Elongate relict BO chondrule in a fine-grained matrix. Ol: Olivine. Px: Pyroxene. M: Fe–Ni metals. Tr: Troilite. Gl: Glass. Chr: Chromite. Merr: Merrillite.

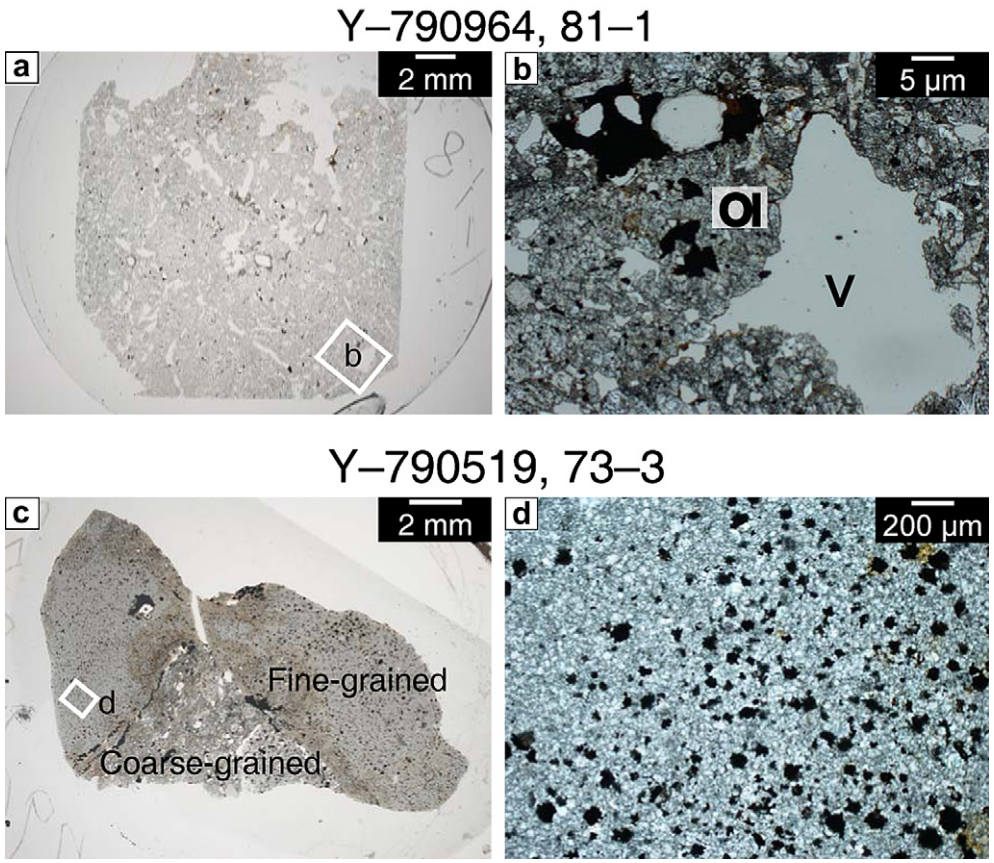

Fig. 11. Photographs of polished thin sections of shock-melted LL chondrites (transmitted light). (a) Low-magnification image of Y−790964, 81−1, showing numerous vugs. The white rectangle indicates the area shown in (b). (b) Close-up image of Y−790964, showing relict olivine fragments and fine-grained olivine. Y−790964 (LL) has similar texture to that of Y−790519 (LL) CG lithology and Y−791088 (H). (c) Low-magnification image of Y−790519, 73−3, showing a fine-grained lithology (mobilized melt) and CG lithology (quiescent melt) coexisting in the polished thin section. The white rectangle indicates the area shown in (d). (d) Close-up image of Y−790519, showing a fine-grained lithology with igneous texture, similar to LAP 02240. The image shows numerous fine-grained olivine and Fe−Ni metal droplets with interstitial glass. Ol: olivine. V: vug.

veins consisting of mixtures of Fe−Ni metals and troilite occasionally occur at the boundary between the completely shock-melted portion and the unmelted host chondrite (Fig. 1f), resulting in segregation of silicate melts and Fe−Ni−FeS melts. The FG lithologies of Y−790519 and LAP 02240 are referred to as "mobilized-melt" type.

As discussed in the previous section, we classified Y−790964, Y−790519 CG, and Y−791088 shock melts as quiescent-melt type. Relict low-Ca pyroxenes occur in Y−791088 (Fig. 2e) but not in the shock-melted LL chondrites, suggesting that the degree of shock-melting in Y−791088 was lower or that the duration of shock-pulse was shorter than that in the case of the shock-melted LL chondrites. The texture of the Ramsdorf L chondrite is similar to that of Y−791088, indicating that Ramsdorf experienced shock melting under similar shock conditions to those recorded by Y−791088. In Ramsdorf, the degree of melting is relatively high, and relict phases are relatively rare, suggesting that near-complete melting occurred (Yamaguchi et al., 1999). This result indicates that the textures of the two types of shock melts were not simply controlled by the degree of shock melting, they were also influenced by the degree of shear stress.

4.3. Geological setting of shock-melted ordinary chondrites

The melting features of Y−791088 and LAP 02240 are similar to those of the impact melts of Y−790964 and the FG lithology of Y−790519, respectively, although differences are seen in the ages of shock melting. Despite the differences in the parent bodies (i.e., the chemical group of the chondrites), the formation processes of the two types of impact-melt rocks (i.e. the quiescent and

mobilized melts proposed in the present study) are analogous. When a large projectile with a hypervelocity (several kilometers per second) collides with an ordinary chondrite parent body to form an impact crater, shock melting of surface rocks may occur near the center of the impact crater (e.g., Melosh, 1984; Stöffler et al., 1991). Shock pressures of 75–90 GPa would be required to cause whole-rock melting (Stöffler et al., 1991). Porosity is an important factor in controlling the amount of impact melt on planetary surfaces (Schaal et al., 1979). Shock-recovery experiments have shown that porous chondritic materials melt at a lower shock-pressure than do massive materials, and extensive shock melting could occur at a relatively low shock-pressure of 45–65 GPa for porous chondritic materials (Hörz et al., 2005; Kitamura et al., 1992). Thus, impact melting would be effective on the regolith surface of chondrite parent bodies.

The opaque vein and elongated chondrule in LAP 02240 are observed at the boundary between the impact melt and the host chondrite. Small dikes or thick melt veins surrounded by unmelted chondritic materials may have cooled rapidly, as suggested by Stöffler et al. (1991) and Bogard et al. (1995). Quiescent and mobilized melts coexist in Y–790519, indicating that the two types of shock melting could have occurred in a thin melt-dike (several to tens of centimeters) or a thick melt vein (Fig. 12).

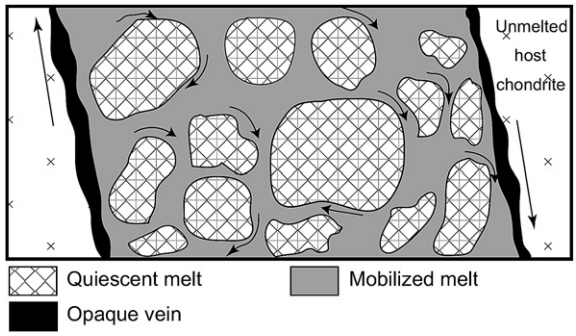

Fig. 12. Geological model explaining the origin of shock-melted ordinary chondrites. Both mobilized and quiescent melts formed in thin dikes or thick veins (several to tens of centimeter thick). Cooling was most rapid at the periphery of the vein, close to the cold host chondrite, where opaque veins formed (as observed in LAP 02240). Mobilized melt and quiescent melt coexist in the dike or vein (Y–790519). The lack of mechanical deformation and relatively slow cooling (or annealing) in the dike resulted in the formation of quiescent melt. The difference between the two types of melt was possibly controlled by the degree of shear stress. Arrows show the direction of movement.

4.4. Thermal conditions of Y–791088 and LAP 02240

4.4.1. Quiescent melts in Y–791088

Y–791088 contains abundant relict olivines and pyroxenes, indicating a maximum temperature of up to ~1500 °C (i.e., close to the liquidus temperature of pyroxene). Because the grain sizes of olivine crystallized from shock melt in Y–791088 (~20 μm) are coarser than those in the case of LAP 02240 (~5 μm), the quiescent melts of Y–791088 might have initially cooled more slowly than those of LAP 02240. In the case that quiescent melts formed in the interior of a dike, undeformed pseudomorphed chondrules, as well as two types of glasses, could be preserved.

4.4.2. Mobilized melts and opaque veins

Once the shock-melts were mobilized, opaque veins of Fe–Ni metals and troilite could have formed along the host–melt contact region due to silicate melt/metal-sulfide melt immiscibility, as observed in LAP 02240 (Fig. 1d and Fig. 12; Stöffler et al., 1991) and in the PAT 91501 shock-melted L chondrite (Benedix et al., 2008; Mittlefehldt and Lindstrom, 2001). The rapid cooling rate estimated for LAP 02240 (~10 °C/s; Cheek and Kring, 2008) is consistent with the fine-grained textures of mobilized melt observed in the present study.

5. Summary

Mineralogical and petrological analyses revealed the formation conditions of two types of shock-melted H chondrites: Y–791088, which formed under quiescent conditions, and LAP 02240, which formed under mobilized conditions. The melting features of Y–791088 and LAP 02240 are similar to those of Y–790964 (LL) and the fine-grained lithology of Y–790519 (LL), respectively. The quiescent and mobilized melts could have solidified under the same conditions as seen in Y–790519 (LL), which formed in a thin dike or thick melt vein. The textures of the two types of shock melts were not simply controlled by the degree of shock melting: they were also influenced by the degree of shear stress.

Acknowledgments

We are grateful to the NASA Meteorite Working Group for providing the sample of LAP 02240. We also thank Drs. K. Righter, M. Kimura, T. Noguchi, and N. Tomioka for providing useful information on shock-melted ordinary chondrites, and Dr. L. E. Nyquist for making valuable comments regarding the manuscript. Substantive reviews by Alan Rubin and an anonymous reviewer improved and clarified the paper.

We are grateful to associate-editor T. Noguchi for his judicious handling of the manuscript. This research was partly supported by NIPR Project Funds, No. 8 (Evolution of the Early Solar System Materials). This work was supported in part by the Center for the Promotion of Integrated Sciences (CPIS) of Sokendai.

References

Bence, A.E., Albee, A.L., 1968. Empirical correction factors for the electron microanalysis of silicate and oxides. J. Geol. 76, 382–403.

Benedix, G.K., Ketcham, R.A., Wilson, L., McCoy, T.J., Boagrd, D.D., Garrison, D.H., Herzog, G.F., Xue, S., Klein, J., Middleton, R., 2008. The formation and chronology of the PAT 91501 impact-melt L chondrite with vesicle–metal–sulfide assemblages. Geochim. Cosmochim. Acta 72, 2417–2428.

Bogard, D.D., Garrison, D.H., Norman, M., Scott, E.R.D., Keil, K., 1995. ^{39}Ar–^{40}Ar age and petrology of Chico: large-scale impact melting on the L chondrite parent body. Geochim. Cosmochim. Acta 59, 1383–1399.

Cheek, L.C., Kring, D.A., 2008. Cooling rate determination for H chondrite impact melt breccia LAP 02240. In: 39th Lunar Planetary Science Conference, #1169 (abstract).

Dodd, R.D., 1981. Meteorites, a Petrologic-Chemical Synthesis. Cambridge University Press, New York.

Folco, L., Bland, P.A., D'Orazio, M., Franchi, I.A., Kelley, S.P., Rocchi, S., 2004. Extensive impact melting on the H-chondrite parent asteroid during the cataclysmic bombardment of the early solar system: evidence from the achondritic meteorite Dar al Gani 896. Geochim. Cosmochim. Acta 68, 2379–2397.

Fujimaki, H., Ishikawa, K., Kojima, H., Yanai, K., Aoki, K., 1993. Rb-Sr age of an impact event recorded in Yamato–791088 H chondrite. In: Proc. NIPR Symp. Antarct. Meteorites, vol. 6, pp. 364–373.

Hörz, F., Cintala, M.J., See, T.H., Le, L., 2005. Shock melting of ordinary chondrite powders and implications for asteroidal regoliths. Meteorit. Planet Sci. 40, 1329–1346.

Kimura, M., Hiyagon, H., Palme, H., Spettel, B., Wolf, D., Clayton, R.N., Mayeda, T.K., Sato, T., Suzuki, A., Kojima, H., 2002. Yamato 792947, 793408 and 82038: the most primitive H chondrites, with abundant refractory inclusions. Meteorit. Planet Sci. 37, 1417–1434.

Kitamura, M., Tsuchiyama, A., Watanabe, S., Syono, Y., Fukuoka, K., 1992. Shock recovery experiments on chondritic materials. In: Syono, Y., Manghnani, M.H. (Eds.), High-pressure Research: Application to Earth and Planetary Science. Geophysical Monograph, vol. 67. Terrapub., AGU, pp. 333–340.

Kring, D.A., Swindle, T.D., Britt, D.T., Grier, J.A., 1996. Cat Mountain: a meteoritic sample of an impact-melted asteroid regolith. J. Geophys. Res. 101, 29353–29371.

Kring, D.A., Hill, D.H., Gleason, J.D., Britt, D.T., Consolmagno, G.J., Farmer, M., Wilson, S., Haag, R., 1999. PortalesValley: a meteoritic sample of brecciated and metal-veined floor of an impact crater on an H-chondrite asteroid. Meteorit. Planet Sci. 36, 439–457.

Krot, A., Ivanova, M.A., Wasson, J.T., 1993. The origin of chromatic chondrules and the volatility of Cr under a range of nebular conditions. Earth. Planet. Sci. Lett. 119, 569–584.

Melosh, M.J., 1984. Impact ejection, and the origin of meteorites. Icarus 59, 234–260.

Mittlefehldt, D.W., Lindstrom, M.M., 2001. Petrology and geochemistry of Patuxent Range 91501, a clast-poor impact melt from the L-chondrite parent body and Lewis Cliff 88663, an L7 chondrite. Meteorit. Planet Sci. 36, 439–457.

Norman, M.D., Mittlefehldt, D.W., 2002. Impact processing of chondritic planetesimals: siderophile and volatile element fractionation in the Chico L chondrite. Meteorit. Planet Sci. 37, 329–344.

Okano, O., Misawa, K., Nakamura, N., Honma, H., Goto, H., 1984. A preliminary study of Rb-Sr systematics and trace element abundances on impact-melted LL- chondrites from Antarctica. Mem. NIPR 35, 285–297. special issue.

Okano, O., Nakamura, N., Nagao, K., 1990. Thermal history of the shock-melted Antarctic LL-chondrites from the Yamato-79 collection. Geochim. Cosmochim. Acta 54, 3509–3523.

Rubin, A.E., 1995. Fractionation of refractory siderophile elements in metal from the RoseCity meteorite. Meteoritics 30, 412–417.

Rubin, A.E., Ulff-Møller, F., Wasson, J.T., Carlson, W.D., 2001. PortalesValley meteorite breccia: evidence for impact-induced melting and metamorphism of an ordinary chondrite. Geochim. Cosmochim. Acta 65, 323–342.

Ruzicka, A., Killgore, M., Mittlefehldt, D.W., Fries, M.D., 2005. PortalesValley: petrology of a metallic-melt meteorite breccia. Meteorit. Planet. Sci. 40, 261–295.

Sato, G., Takeda, H., Yanai, K., Kojima, H., 1982. Impact-melted LL-chondrites of Yamato 79-collection. 7th Symp. Antarctic Met., pp. 9–10.

Satterwhite, C., Righter, K., 2004. Antarctic Meteorite News Letter 27, Number 3. NASA Johnson Space Center, Houston.

Schaal, R.B., Hörz, E., Thompson, T.D., Bauer, J.F., 1979. Shock metamorphism of granulated lunar basalt. In: Proc. 10th Lunar Planet. Sci. Conf., pp. 2574–2571.

Scott, E.R.D., Taylor, G.J., 1983. Chondrules and other components in C, O and E chondrites: similarities in their properties and origins. J. Geophys. Res. 88 (Suppl), B275–B286.

Stöffler, D., Keil, K., Scott, E.R.D., 1991. Shock metamorphism of ordinary chondrites. Geochim. Cosmochim. Acta 55, 3845–3867.

Yamaguchi, A., Scott, E.R.D., Keil, K., 1998. Origin of unusual impact melt rocks, Yamato-790964 and -790143 (LL-chondrites). Antarctic Meteorite Res. 11, 18–31.

Yamaguchi, A., Scott, E.R.D., Keil, K., 1999. Origin of a unique impact-melt rock – the L-chondrite Ramsdorf. Meteorit. Planet Sci. 34, 49–59.

Yanai, K., Kojima, H., 1995. Catalog of the Antarctic Meteorites. Nat. Inst. Polar Res., Tokyo.

Yolcubal, I., Sack, R.O., 1997. Formation conditions of igneous regions in ordinary chondrites: Chico, RoseCity, and other heavily shocked H and L chondrites. J. Geophys. Res. 102, 21589–21611.

NiPR
National Institute of Polar Research

INTERNATIONAL POLAR YEAR 2007-2008